Detailed Nonlinear Modeling and High-Fidelity Parallel Simulation of MMC With Embedded Energy Storage for Wind Farm Grid Integration

BINGRONG SHANG[1] **(Member, IEEE), NING LIN**[2] **(Member, IEEE),
AND VENKATA DINAVAHI**[1] **(Fellow, IEEE)**

[1]Department of Electrical and Computer Engineering, University of Alberta, Edmonton, AB T6G 2V4, Canada
[2]Powertech Labs Inc., Surrey, BC V3W 7R7, Canada

CORRESPONDING AUTHOR: B. SHANG (bingrong@ualberta.ca)

ABSTRACT Integration of renewable energy is increasingly prevalent, yet its stochasticity may compromise the stability of the power system. In this paper, a high-voltage dc (HVDC) link model based on the modular multilevel converter with embedded energy storage (MMC-EES) is presented and, utilizing the massively parallel computing feature of the graphics processing unit (GPU), its efficacy in compensating a varying wind energy generation is studied. Constant power is oriented in the inverter control by incorporating a DC-DC converter with EES into its submodules. High-fidelity electromagnetic transient modeling is conducted for insights into converter control and energy management. A fully iterative solution is carried out for the nonlinear model for high accuracy. Since the sequential data processing manner of the central processing unit (CPU) is prone to an extremely long simulation following an increase of component quantity with even one order of magnitude, the massively concurrent threading of the GPU is exploited. The computational challenges posed by the complexity of the MMC circuit are effectively tackled by circuit partitioning which separates nonlinearities. In the meantime, components of an identical attribute are designed as one kernel despite inhomogeneity. The proposed modeling and computing method is applied to a multi-terminal DC system with wind farms, and significant speedups over CPU-based simulation are achieved, with the accuracy validated by the offline simulation tool PSCAD.

INDEX TERMS Energy storage system, graphics processors, high voltage direct current, modular multilevel converter, nonlinear systems, parallel processing, power system stability, supercapacitor, wind farm.

LIST OF ABBREVIATIONS

CCM	Continuous Conduction Mode.
CPU	Central Processing Unit.
DCM	Discontinuous Conduction Mode.
EMT	Electromagnetic Transients.
GPU	Graphic Processing Unit.
HBSM	Half-Bridge Submodule.
HVDC	High-Voltage Direct Current.
IGBT	Insulated Gate Bipolar Transistor.
MMC	Modular Multi-Level Converter.
MMC-EES	MMC with Embedded Energy Storage.
PCC	Point of Common Coupling.
SIMT	Single Instruction Multiple-Thread.
SM	Submodule.
SM-ES	Submodule with Energy Storage.
SoC	State of Charge.

I. INTRODUCTION

WIND has become a major resource for renewable energy generation because of ecological and environmental benefits. As the technology is mature, a wind farm can be constructed within a short cycle at a comparatively low cost [1]. However, wind power is unstable because the strength and direction of the natural wind are stochastic, bringing dramatic challenges to the stability of the power

grid [2] when there is large-scale wind energy penetration. In such cases, power electronics-based energy storage systems as a solution can quickly provide a continuous and stable backup power supply to avoid economic losses [3].

Energy storage systems can be deployed in a centralized or distributed form. The high modularity and flexibility of the latter type make it more competitive than its centralized counterpart [4], and thus increasingly utilized [5], [6]. As an alternative to lithium batteries, energy storage based on supercapacitors has drawn attention in power apparatus, such as the wind turbine [7], and the shipboard power system [8] for advantages such as faster and safer charging, more eco-friendly raw materials, and longer lifetime. Supercapacitors can also be adopted as split energy storage elements to AC-DC converters as fault-resilient schemes [9]. In a simulated onboard network, they are also chosen to serve as storage systems due to their fast dynamics and decent efficiency [10].

The modular multilevel converter (MMC) has grown rapidly in recent years and is widely adopted in high-voltage direct current (HVDC) for offshore wind farm integration [11], [12]. An MMC with embedded energy storage (MMC-EES) would facilitate the distribution of numerous batteries or supercapacitors among its submodules and therefore enables more effective energy management. Electromagnetic transient (EMT) simulation plays an important role in the study of such kinds of power electronics apparatuses applied in power systems prior to in-situ commissioning. To expedite the simulation, the average-value models [13] and equivalent models [14] are adopted for MMC-EES. As a consequence, the simulation omits transient electromagnetic details of individual components which are crucial for a design evaluation.

The detailed model, on the other hand, can demonstrate the dynamics of each submodule (SM) accurately. For example, the detailed model of MMC [15] yields results that agree with the experiments. For the simulation of massive MMC-EES systems, practical challenges include a large time-varying admittance matrix brought by the converter, a small step size owing to the high switching frequency required by the submodule with energy storage (SM-ES), and Newton-Raphson iterations demanded by the nonlinear component insulated gate bipolar transistor (IGBT). The central processing unit (CPU) will be easily overwhelmed by these factors if sequential processing is carried out. Therefore, the extremely slow simulation speed prompts the exploration of hardware parallelism, in which case the application of hardware computational acceleration such as Field Programmable Gate Array (FPGA) [16] has a distinct effect. However, for multi-terminal complicated systems, FPGA is deficient in terms of digital hardware resources to accommodate practical large-scale circuits and systems.

Attributing to its massive number of cores which enables a concurrent and efficient execution of a substantial number of threads, the graphics process unit (GPU) is promising in the high-performance computing of various electrical energy systems with explicit homogeneity [17]. It has been employed for EMT simulation acceleration of large-scale AC and DC grids [18], [19], [20] where dozens to hundreds of speedups over single-core and multi-core CPUs were gained. The single-instruction multiple-thread (SIMT) feature of GPU is also suitable for transient stability analysis of homogeneous power systems [21]. Furthermore, leveraging the computational resources by C++ and CUDA C++ programming, the GPU starts to be utilized for dealing with homogeneity in conjunction with inhomogeneity by the CPU in hybrid EMT and dynamic simulations [22], [23]. Hitherto, the GPU has been primarily used to process identical units such as the MMC [24], [25], and there has been a notable scarcity of efforts dedicated to the parallel simulation of inhomogeneity in power systems and circuits such as a combination of both MMC and MMC-EES, despite the fact that it remains a significant challenge.

In this work, a detailed EMT model of MMC-EES is proposed and high-performance electromagnetic transient simulation using a fully iterative solution scheme is conducted on the GPU, thereby contributing to the field of GPU-accelerated power system simulation. The operation modes are analyzed and the performance of the controller is demonstrated by MMCs with a proper voltage level. The pursuit of high-fidelity simulation, particularly for applications such as energy management in energy storage units, necessitates the detailed modeling of numerous submodules and the analysis of individual capacitor states. This requirement vastly exceeds the computational capacity of conventional CPUs. Consequently, our investigation delves into the parallel processing capabilities of GPUs to embark on a substantial simulation endeavor. Moreover, the nonlinearity caused by power semiconductor switches is excluded from the MMC main circuit so that both can be processed more efficiently. Recognizing that inhomogeneity poses a significant challenge for parallel processing on GPU, this work is strategically oriented toward developing methodologies that enhance homogeneity, leading to an additional acceleration factor, even though it is absent in the MMC-EES as a single circuit.

This paper is organized as follows. Section II introduces the topology and control strategy of the MMC with embedded energy storage. In Section III, the EMT model of the MMC-EES is presented. The design of the GPU parallelism is provided in Section IV. Section V gives the implementation results and the validation, and conclusions are drawn in Section VI.

II. MODELING AND CONTROL OF MMC-EES
A. TOPOLOGY OF MMC-EES
The configuration of a 3-phase MMC is shown in Fig. 1, where each phase consists of two bridge arms, both of which are composed of cascaded submodules in series with an inductor denoted as L_u or L_d.

Fig. 2(a) shows the submodule structure of an MMC with embedded energy storage, which is a combination of the conventional half-bridge submodule (HBSM) and a DC-DC converter with an array of supercapacitors on the low
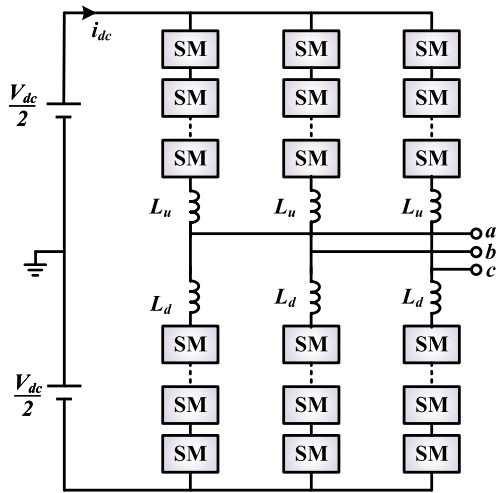
FIGURE 1. Topology of a three-phase modular multilevel converter.

voltage side. The HBSM consists of two complementary power switches S_1 and S_2 and a capacitor C_{sm}. The amount of energy that can be stored in C_{sm} is relatively small and insufficient to serve as a grid energy supply.
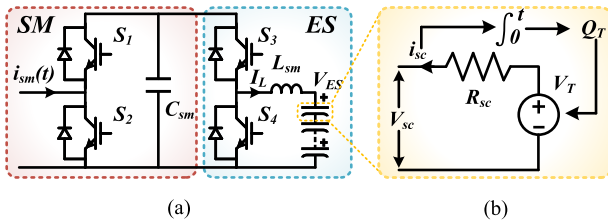
FIGURE 2. (a) SM-ES topology; (b) supercapacitor equivalent circuit.

In contrast, the SM-ES has a number of energy storage units and a DC-DC converter connected in parallel with the capacitor C_{sm}. The bi-directional DC converter allows the charge and discharge of supercapacitors. To be specific, the converter operates as a buck converter when the supercapacitors are storing energy, while it turns into a boost circuit to provide energy to the external system. Since all the energy storage units can be equally distributed, the power rating of each SM-ES is significantly lower compared with the entire MMC. This implies that a high switching frequency can be attained more easily to enhance power density and to reduce the volume of inductor L_{sm}, a high switching frequency is particularly chosen for the two IGBTs S_3 and S_4.

The total amount of energy that three-phase MMC stores could be expressed as

$$W = \frac{1}{2}C_{ES}V_{ES}^2 \times 6N, \tag{1}$$

where C_{ES} and V_{ES} are the equivalent capacitance and voltage of the whole supercapacitor array, respectively, and N is the

number of SMs per arm. With a rated power P_r, the inertia of the MMC [26] can be described as

$$H = \frac{C_{ES}V_{ES}^2 \times 6N}{2P_r}. \tag{2}$$

To facilitate an energy management study in the high-fidelity EMT simulation, each supercapacitor is modeled. The Thévenin equivalent circuit for an individual supercapacitor is shown in Fig. 2(b), and the overall voltage of the array could be calculated as

$$V_{ES} = \sum_{i=1}^{N_{sc}} V_{sc_i}, \tag{3}$$

where N_{sc} is the number of supercapacitors in series, and V_{sc} is the supercapacitor terminal voltage [27]:

$$V_{sc} = \frac{r}{\varepsilon} + \frac{2RT}{F}sinh^{-1}\left(\frac{Q_T}{\sqrt{8RT\varepsilon c}}\right) - R_{sc}i_{sc}, \tag{4}$$

R_{sc} is the equivalent resistance, i_{sc} is the supercapacitor current, R is the ideal gas constant, T is the operating temperature, F is the Faraday constant, r is the molecular radius, c is the Molar concentration, ε is the permittivity of the material, and Q_T is the electric charge which is determined by the supercapacitor current

$$Q_T = \int_0^t i_{sc}dt. \tag{5}$$

The state of charge (SoC) of a supercapacitor is defined as the ratio between the remaining capacity and the rated capacity. A zero SoC means the supercapacitor is completely discharged while it is 100% for a fully charged supercapacitor. It is formulated as follows

$$SoC = (SoC_{init} - \frac{Q_T}{Q}) \times 100\%, \tag{6}$$

where SoC_{init} is the initial SoC, and Q is the rated capacity of the supercapacitor.

Regardless of the energy flow direction, the continuous conduction mode (CCM) is always desired for energy storage units such as batteries and supercapacitors. Otherwise, they will be subject to frequent charge and discharge if under the discontinuous conduction mode (DCM), which not only affects the efficiency but also the lifetime of the energy storage devices. To maintain the CCM, the critical value of the inductor needs to be determined. When the DC-DC converter operates under the boost mode, the current ripple of the inductor Δi_L could be expressed as

$$\Delta i_L = \frac{V_{ES}}{L_{sm}f_{ES}}D \tag{7}$$

where D is the duty cycle, and f_{ES} is the switching frequency of S_3 and S_4. Substituting D with variables that can be monitored leads to

$$\Delta i_L = \frac{V_{ES}(V_{C_{sm}} - V_{ES})}{L_{sm}f_{ES}V_{C_{sm}}} \tag{8}$$

where $V_{C_{sm}}$ is the instantaneous voltage of C_{sm}.

In the meantime, the DC component of the inductor I_L can be determined from measurable quantities including the power provided or consumed by the submodule P_{sm}, i.e.,

$$I_L = \frac{P_{sm}}{V_{ES}} \tag{9}$$

To maintain CCM, the peak-to-peak current ripple should be smaller than 2 times of I_L, which consequently yields the critical inductance

$$L_{crit} = \frac{V_{ES}^2(V_{C_{sm}} - V_{ES})}{2P_{sm}f_{ES}V_{C_{sm}}}. \tag{10}$$

Similarly, analysis of the ripple current under the buck mode yields the same critical inductance. Then, the final value of L_{crit} is chosen based on a number of factors, including the operational voltage range of the supercapacitor array, the maximum allowed charging or discharging power, as well as the submodule voltage scale. When $L_{sm} > L_{crit}$, the supercapacitors will be charged or discharged continuously; otherwise, they will encounter frequent interruptions that affect their capacity and lifetime.

B. CONSTANT POWER CONTROL

Fig. 3 shows the integration of two wind farms into a distribution network via the multi-terminal DC grid. The MMC-EES is located at the grid side as an inverter, and the conventional HBSM-based MMC operates as a grid-forming rectifier which provides a stable voltage at the point of common coupling (PCC) for offshore wind farms. The wind farm side and the grid side converters are linked by the transmission lines TL_1 and TL_2, and TL_3 connects the two grid-side MMCs to form a multi-terminal DC system.

FIGURE 3. Multi-terminal DC grid with MMC-EES for wind farm integration.

For a lumped wind farm model that has N_{wf} wind turbines, its total output power P_{wf} can be calculated as

$$P_{wf} = \frac{1}{2}Av^3C_p\rho\eta \times N_{wf}. \tag{11}$$

where A is the wind sweep area, v is the wind speed, C_p is the wind energy conversion rate value, ρ is the air density, and η is the coefficient. As the power delivered from the rectifier is not constant, the inverter MMC needs to supplement or absorb extra energy to keep the desired import power into the distribution grid, i.e., the balance between the power feeding

into the grid and the power in the DC yard is maintained by the power of the MMC-EES.

The two control methods of MMC-EES as an inverter and the grid-forming MMC as a rectifier are shown in Fig. 4(a). The rectifier is expected to provide a stable voltage for wind turbines. The PCC voltages after *abc-dq* transformation are compared with their references v_{gd}^* and v_{gq}^* and then the errors are regulated by subsequent PI controllers to yield the current references i_d^* and i_q^*. On the other hand, the inverters are in charge of establishing the DC voltage, the d-axis reference current i_d^* comes from regulation of the DC voltage v_{dc}, and the q-axis reference current i_q^* is related to reactive power or bus voltage control. The inner-loop current control remains identical regardless of converter types. The modulation signals m for 3 phases are generated after the dq-abc transformation. The angle reference θ is predefined without the usage of a phase-locked loop for the grid-forming MMC, whereas it is calculated based on the 3-phase grid voltage for an inverter.

(a)

(b)

FIGURE 4. MMC control scheme: (a) Outer loop control; (b) coordinated submodule dc voltage and power control.

Fig. 4(b) demonstrates the submodule internal controller, which includes regulations of capacitor voltage and super-capacitor power, respectively. The control of capacitor C_{sm} voltage in an MMC SM is shown in the upper part of Fig. 4(b), which is divided into average control and balance control [28]. The actual capacitor voltage v_c is compared with its reference v_c^* in the balance control, and the result is added up with that of average control denoted by v_{au}, as well as the phase reference signal which links the internal controller to

its outer-loop counterpart and takes the form of

$$u_{refp} = \frac{V_{dc}}{2N} - m, \tag{12}$$

where V_{dc} is the converter DC voltage. As can be seen, the first two switches denoted as S_1 and S_2 are the objectives of the control scheme.

The second controller in Fig. 4(b) is designed for the DC-DC circuit with embedded energy storage for power compensation at the converter level. Since it independently controls the turn-on and turn-off of the remaining two switches S_3 and S_4, the switching frequency, denoted as f_{ES}, can be much higher than that of the carrier in the first PWM scheme. In the meantime, the switch ON and OFF commands for upper and lower IGBTs are opposite to that of the MMC submodule. The set power reference of the entire MMC P^* is distributed equally among the SMs with energy storage so that P^*_{sm}, the reference power for each SM, can be derived as

$$P^*_{sm} = \frac{P^* - (V_{dc}I_{dc})}{6N}, \tag{13}$$

where I_{dc} is the converter-side current.

When there is a power shortage or surplus due to disturbance in the wind farm, the MMC-EES is able to provide stable power as a backup plant in this control strategy so long as the complement is within its capacity.

III. MMC EMT MODEL OPTIMIZATION

The detailed electromagnetic transient modeling of the MMC-EES is essential for a comprehensive design evaluation since it provides insight into the converter operation status. Tremendous computational resources are generally required when the simulation of a grid-connected high-level MMC modeled in its full scale is carried out. The consequent heavy computational burden is first tackled by circuit size reduction which results in the separation of submodules from the MMC main circuit, as depicted on the left side of Fig. 5.

Since the frequency of the arm current is much lower than the EMT simulation frequency, it can be considered as a constant for two adjacent time steps, and therefore the SM can be separated from the arm and forms a single subsystem by inserting one step latency between the voltage and current sources. The MMC main circuit becomes linear since after the exclusion of all SMs, the arm is comprised of voltage sources v_{pn}, where n is from 1 to N, in addition to an inductor. On the nonlinear SM side, the current injected into it is equal to the arm current in the previous time step.

A. NONLINEAR SUBMODULE SPLITTING

The Norton equivalent circuit of the submodule with energy storage is shown in Fig. 5, where each nonlinear power switch is discretized and represented by a current source f_i (i = 1 - 4) in parallel with conductance G_i.

To reflect an accurate performance of the IGBT, the free-wheeling diode is normally taken into consideration, which indicates the power semiconductor switch model is

a combination of both. The gate signal g determines the switching state of this combination. When the switch is turned on, the conductance is $1/r_{on}$ and the voltage drop v_{on} which can be reliant on the collector current. When the diode is under conduction, i.e., the ideal diode D_0 is on, the total voltage drop is induced by the p-n junction voltage V_j and the resistor r_{on}. The internal voltage drop of the IGBTs and diode device results in the companion currents, i.e., f_1, f_2, f_3, and f_4.

Circuit partitioning of the MMC significantly reduces the number of nodes on both sides, as the submodule only has 5 nodes. The node voltage vector $\mathbf{v_{SM}}$ in SM-ES could be obtained by

$$\mathbf{v_{SM}} = \mathbf{G_{SM}^{-1}} \cdot \mathbf{J_{SM}}. \tag{14}$$

Since each submodule constitutes an independent circuit, an extra node can be omitted. By taking Node 0 as a virtual ground, the original 5th-order matrix is reduced to 4th-order. Then, the 4×4 admittance matrix $\mathbf{G_{SM}}$ can be organized as:

$$\begin{bmatrix} G_C + G_1 + G_3 & -G_1 & -G_3 & 0 \\ -G_1 & G_1 + G_2 & 0 & 0 \\ -G3 & 0 & G_L + G_3 + G_4 & -G_L \\ 0 & 0 & -G_L & G_L + G_{es} \end{bmatrix} \tag{15}$$

and the companion current vector is

$$\mathbf{J_{SM}} = \begin{bmatrix} I_{Ceq} + f_1 + f_3 \\ J_s - f_1 + f_2 \\ I_{Leq} - f_3 + f_4 \\ -I_{Leq} + I_{es} \end{bmatrix} \tag{16}$$

In the matrices $\mathbf{G_{SM}}$ and $\mathbf{J_{SM}}$, the transmission line model (TLM) technique [29] is deployed to model reactive components, i.e., capacitors and inductors, as transmission line stubs, where the characteristic impedance are $Z_C = dt/(2C)$ and $Z_L = (2L)/dt$, respectively, and equivalent current injection value in the SM-ES are

$$I_{Ceq} = \frac{2v_C^i}{Z_C}, I_{Leq} = \frac{2v_L^i}{Z_L}, \tag{17}$$

and J_s is the arm current.

In order to improve the efficiency of circuit simulation, the supercapacitor units are placed in a separate function to calculate the equivalent conductance G_{es} and equivalent current source I_{es} before using them as elements of the matrix for the next step, where

$$G_{es} = \frac{1}{\sum_{i=1}^{N_{sc}} R_{sc}}, \tag{18}$$

and

$$I_{es} = G_{es} \sum_{i=1}^{N_{sc}} \left(\frac{r}{\varepsilon} + \frac{2RT}{F} sinh^{-1} \left(\frac{Q_T}{\sqrt{8RT\varepsilon c}} \right) \right). \tag{19}$$

The $\mathbf{G_{SM}}$ and $\mathbf{J_{SM}}$, along with the input current source J_s, are involved in the circuit solution. The solution of (14) is iterative because of the diode nonlinearity, with the history terms not updated until the solution converges.
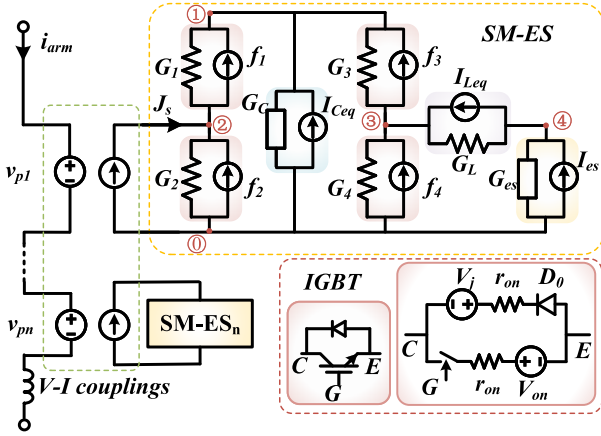
FIGURE 5. MMC partitioning by *V-I* couplings and SM with embedded energy storage equivalent model.

B. MMC CONSTANT ADMITTANCE CIRCUIT

Following the splitting of submodules, each arm in the MMC main circuit only consists of cascaded voltage sources v_{pi} ($i = 1$ to N) along with an inductor, which takes the form of a Thévenin equivalent circuit and therefore, can be transformed into its Norton counterpart.

The arm voltage could be derived as

$$v_{arm}(t) = \left(\sum_{i=1}^{N} v_{pi}(t - \Delta t) + 2v_{L_{u/d}}^{i}(t) \right) + (Z_{L_{u/d}} + R_{arm})i_{arm}(t), \qquad (20)$$

where $vi_{L_{u/d}}$ and $Z_{L_{u/d}}$ are the incident pulse and impedance of the inductor on the bridge arm as the TLM stub model, respectively, and R_{arm} is the parasitic resistance of the inductor.

The equivalent conductance and companion current of an arm can be expressed as follows,

$$G_{eq} = \frac{1}{Z_{L_{u/d}} + R_{arm}}, \qquad (21)$$

and

$$I_{eq} = (\sum_{i=1}^{N} v_{pi} + 2v_{L_{u/d}}^{i})G_{eq}. \qquad (22)$$

Depending on the role of the MMC, its AC side is connected to either a distribution grid that has a stiff voltage or a wind farm that is modeled as a current source. The AC side always accounts for 3 nodes irrespective of the converter function. Then, with the transmission line on its DC side, one converter station can be separated from another and a constant admittance matrix with a minimum dimension of 5 is formed. The arm current I_{arm}, i.e., the terminal current of a submodule J_s, is obtained after solving the corresponding matrix equation of the MMC main circuit and is used for calculating the SM voltages at the next time step.

IV. GPU PARALLEL DESIGN AND IMPLEMENTATION

In this work, the Nvidia® Tesla V100 GPU with 5120 CUDA cores and 16GB HBM2 memory [30] and 20-core Intel® Xeon E5-2698 v4 CPU are adopted for the high-performance computing of the DC grid integrated with wind farms, with a simulation time-step of 2 μs, since the high switching frequency of the DC-DC converter.

A general CUDA program architecture that contains several stages is shown in Fig. 6.
1) Perform data initialization on the CPU termed as the host where global variables are first defined and initialized.
2) Allocate memory for the GPU device to which data from the host are copied via PCI-Express (PCIe).
3) Invoke kernels to perform operations on the device where the time-domain simulation is conducted.
4) Copy the results to be analyzed from the device to the host.
5) Free the allocated memory.
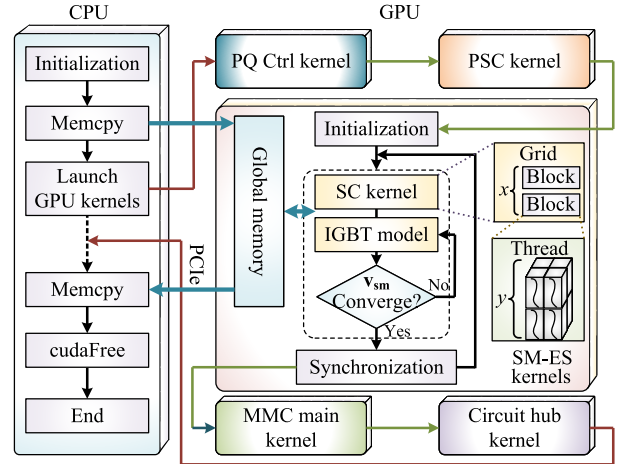
FIGURE 6. GPU simulation process flow chart.

Specifically, in the SM-ES kernel, the IGBT model is programmed as a device function that is called four times, and its outputs are involved in forming (14), which is solved after Newton-Raphson iterations to determine whether $\mathbf{v_{sm}}$ converges. If the result converges, the simulation proceeds to the next time step. Otherwise, the iterations will be repeated.

When a GPU kernel is invoked, it automatically launches a few blocks, with each having an identical number of threads that are specified in the CUDA C++ command. For example, as depicted in Fig. 6, the SC kernel invokes a total number of $x \times y$ threads, each corresponding to a physical component, i.e., a supercapacitor. The block number x and the thread quantity per block y are determined based on the actual number of components in the entire DC system.

Fig. 7 shows massively parallel implementation of various kernels that compose the 4-terminal DC grid integrated with wind farms. All the variables exchanged between kernels are defined and stored in the global memory of the GPU device. Therefore, a global variable is accessible by an arbitrary

thread and can also be exported conveniently to the host for further analysis and data processing.

The supercapacitor kernel *SC* is responsible for calculating the impedance and output voltage of all supercapacitors. Then, the equivalent conductance and companion current composing the Norton circuit of a supercapacitor array in an SM are derived by another kernel *SCsum*. It is noticed that the former kernel has more threads than the latter and their exact numbers could be respectively expressed as

$$N_{SC}^T = \frac{N_{stn}}{2} \times 6N \times N_{sc}, \tag{23}$$

$$N_{SCsum}^T = \frac{N_{stn}}{2} \times 6N, \tag{24}$$

where N_{stn} denotes the station number, which is 4 in this work. Once the *SC* kernel completes the computation, its outputs R_{sc} and V_{sc}, both of which are N_{SC}^T dimensional, are assigned to N_{SCsum}^T groups, in each of which N_{sc} elements are summed up.

Although the multi-terminal DC grid shown in Fig. 3 comprises two types of MMC submodule structures, i.e., the HBSM and the SM-ES, they are written as one *SM* kernel to improve the parallelism since under this circumstance, all submodules can be implemented concurrently despite the inhomogeneity. The two main differences are: the admittance matrix size of the HBSM is 2×2 while the SM-ES is 4×4, which can be solved by invoking the corresponding device function, and the power control strategy for the energy storage module is distinguished by the specific thread ID. Since not every *SM* kernel in the GPU implementation needs the output from the *SC* kernel, memory needs to be allocated reasonably during the GPU kernel programming. As shown at the bottom of Fig. 7, in the 4-terminal system, MMCs numbered 2 and 4 have embedded energy storage. Therefore, in the *SM* kernel, the SC memory address needs to be biased accordingly by the thread ID. The number of threads N_{SM}^T is the same as in (24).

In the meantime, the application of circuit partitioning results in identical MMC main circuits regardless of the roles these converters play in the DC grid because both the three-phase voltage and current sources can be represented by Norton equivalent circuits and all the legs are structurally identical. The AC side can be appropriately differentiated between wind farms and grids by their types, and the computation can be implemented in a SIMT manner by the same kernel *MMC* which has N_{stn} threads.

Since a unified controller is available, the control process of the rectifier and inverter MMCs can also be programmed into the same kernels. The inner loop phase-shift control kernel *PSC*, which is in charge of SM capacitor voltages and does not need to branch off the scheme internally, has a thread quantity N_{PSC}^T equal to $3N_{stn}$. In the outer-loop control kernel *PQ_Ctrl*, the MMC-EES is distinguished from a conventional MMC by its type to maximize the efficiency of GPU implementation with a thread number of N_{stn}.
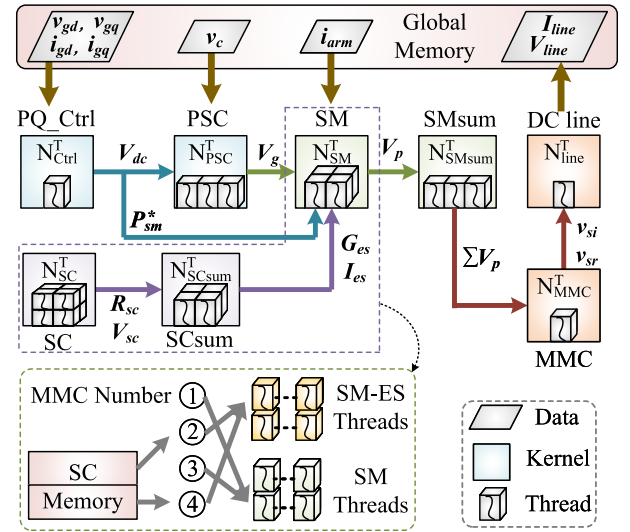

FIGURE 7. Overall GPU program architecture for the transient simulation of the MMC-EES based multi-terminal DC grid.

V. RESULTS AND VALIDATION

The voltage level of a grid-connected MMC should be sufficiently high and therefore, various levels are simulated and the results of a 51-level MMC are provided. The simulation results are compared with the PSCAD^TM results in a number of cases to verify the accuracy. Moreover, a thorough investigation explores the comparative simulation speed involving GPU-based simulation, single-core CPU simulation, and multi-core CPU simulation enhanced by the application of OpenMP pragmas.

The GPU implementation results with the energy storage units being discharged are shown in Fig. 8 and Fig. 9. Fig. 8(a) shows the power of the wind farm, MMC-EES, grid, and transmission line, respectively. When t is 1.0 s, the output power of the wind farm gradually decreases from 160 MW to approximately 100 MW to simulate the situation where the wind speed slows down. In this case, the power on the DC transmission line TL_1 changes in the same trend as the wind farm, and the power provided by MMC-EES increases from 140 MW to 200 MW so that the power on the grid side is able to remain stable at 300 MW. Even during the 0.4 s period when the wind speed is quickly reducing, the distribution grid is still provided a nearly constant 300 MW power attributing to a fast converter response.

The DC voltages of both the inverter and rectifier are presented in Fig. 8(b), where V_{dc1} is the rectifier side voltage while V_{dc2} is from the inverter side. V_{dc1} drops from about 206 kV to 204 kV between 1.0 s and 1.4 s, while the grid side MMC DC voltage V_{dc2} maintains at 200 kV because of its designed function. The voltage difference ΔV between the two sides is reduced from about 6 kV to 4 kV due to the power reduction of the wind farm. In Fig. 8(c), the 3-phase PCC voltage of the offshore wind farm is depicted, and the maximum value of the voltage is maintained exactly at the expected 110 kV.
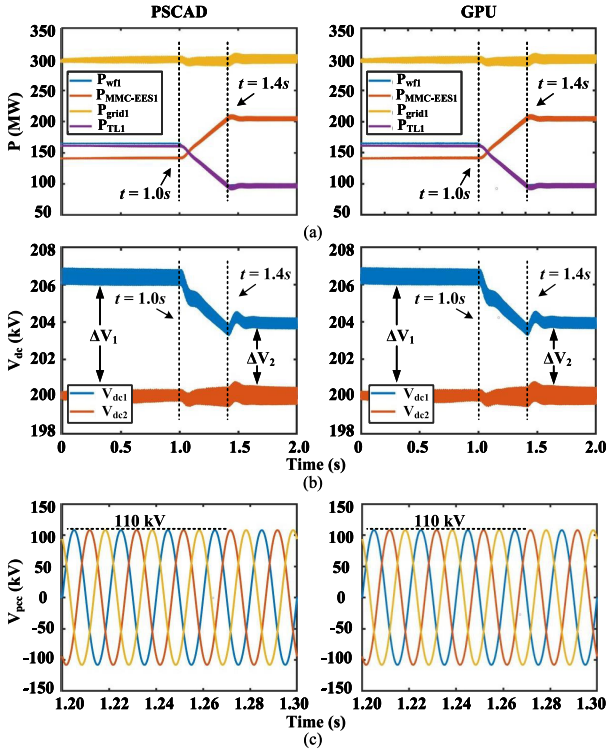
FIGURE 8. PSCAD^{TM} and GPU simulation results of discharging mode: (a) Power of wind farm, MMC-EES, grid and transmission line; (b) DC voltages; (c) wind farm PCC voltage.
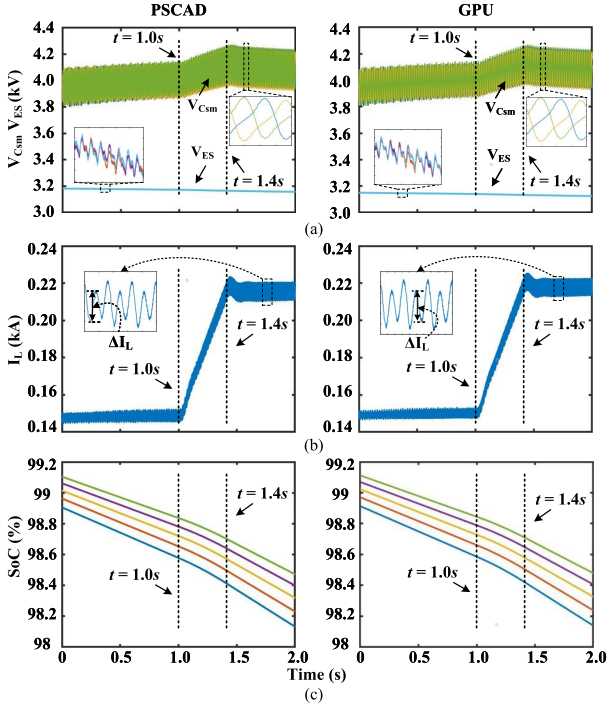
FIGURE 9. PSCAD^{TM} and GPU simulation results of discharging mode: (a) Voltages of capacitor and supercapacitor in SM-ES; (b) DC-DC converter inductor current; (c) SoC of the supercapacitors.

Fig. 9(a) depicts the voltage of the capacitor V_{Csm} and the voltage of the supercapacitor array V_{ES} in one of the SM-

ES for 3 different arms. V_{Csm} increases temporarily from around 3.9 kV to 4.0 kV during the dynamic period, while the voltage of the energy storage module V_{ES} gradually decreases from about 3.18 kV to 3.16 kV as a result of the discharge. As shown in Fig. 9(b), the current of the inductor in an arbitrary SM-ES maintains CCM. As the MMC-EES provides more energy to the distribution grid, the current I_L increases from 0.148 kA to 0.218 kA between 1.0 s and 1.4 s, and the ripple current ΔI_L is about 0.007 kA. Fig. 9(c) illustrates the SoC of five supercapacitors with different initial voltages in an SM-ES. The high-fidelity modeling of each individual supercapacitor can provide more details of the behavior of all the supercapacitor components in the system, enabling improved monitoring and energy management. As can be observed, the supercapacitors discharge faster after $t = 1.0$ s, so the slope becomes steeper and the overall SoC decreases from 99% to 98.4%.

To demonstrate the accuracy of the GPU-based simulation methodology, a detailed numerical comparison plot has been provided. Taking the wind farm power P_{wf1} as an example, the absolute error is calculated as:

$$Error = \frac{|P_{wf1}^{PSCAD} - P_{wf1}^{GPU}|}{P_{wf1}^{PSCAD}} \times 100\%, \qquad (25)$$

where P_{wf1}^{PSCAD} represents the PSCAD^{TM} simulation result and P_{wf1}^{GPU} is obtained from GPU simulation. Fig. 10 (a) depicts the error in the wind farm power P_{wf1} during the simulation process, demonstrating an error not exceeding 0.014%. Fig. 10 (b) shows the overall error of capacitor voltage V_{Csm} at approximately 6% because of a shift of a virtually identical waveform in the time axis. The DC voltage V_{dc1} error is exhibited in Fig. 10 (c), with a maximum value not surpassing 0.004%. Additionally, Fig. 10 (d) characterizes the error of inductor current I_L, showcasing a gradual reduction from an initial 1.6% to 0.4% at $t=1.0$ s.
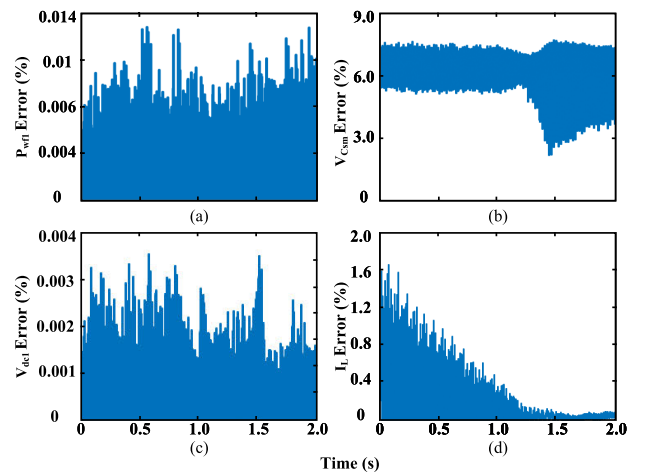
FIGURE 10. Absolute error between GPU and PSCAD^{TM} simulation results: (a) wind farm power P_{wf1} error; (b) capacitor voltage V_{Csm} error; (c) DC voltage V_{dc1} error; (d) inductor current I_L error.

As a common operation scenario of the system, Fig. 11 and Fig. 12 demonstrate the transition between the two states of charging and discharging. In Fig. 11(a), the initial power of the wind farm is still 160 MW, and at 0.4 s, P_{wf1} starts to progressively increase, reaching around 250 MW at 1.4 s. Since the grid-side reference power is set to 200 MW, it can be seen that the output power of MMC-EES1 $P_{MMC-EES1}$ decreased from its initial value of 40 MW to -50 MW at $t = 1.4$ s due to the energy storage system transitioning from discharge mode to charge mode to store the additional amount of energy. Throughout the process, P_{grid1} maintains a stable power level, proving the satisfactory performance of the system in both dynamic and steady-state conditions. It can be seen from Fig. 11(b) that V_{dc1} keeps increasing from 206 kV at 0.4 s to about 209 kV at 1.4 s. The inverter side DC voltage V_{dc2} stabilizes at 200 kV as a result of the DC voltage control of MMC-ES. The DC voltage on the rectifier side becomes larger at 1.4 seconds, i.e., ΔV_2 is almost 4 kV greater than ΔV_1. The wind farm PCC voltages are provided in Fig. 11(c) with the peak value remaining at 110 kV throughout.
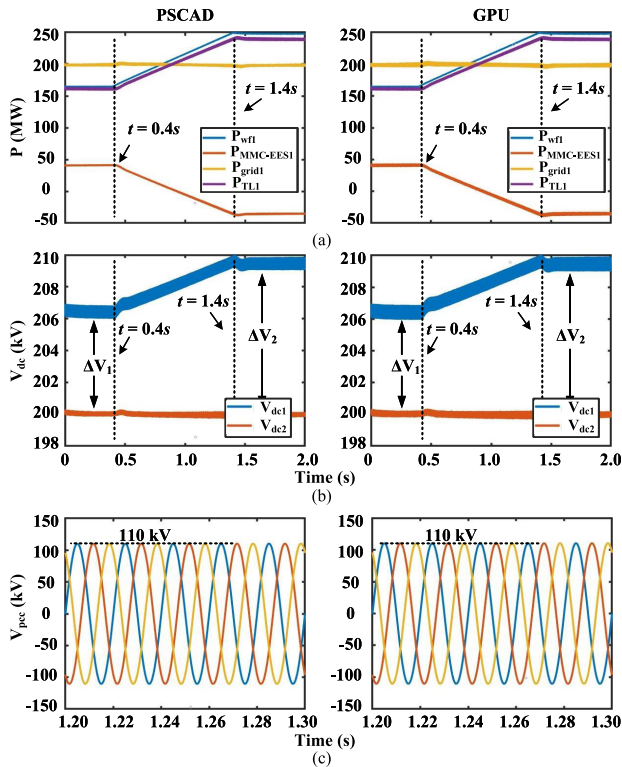
FIGURE 11. GPU and PSCAD^TM simulation results of mode transition: (a) Power of wind farm, MMC-EES and grid; (b) DC voltages; (c) PCC voltage of wind farm.

The V_{Csm} and V_{ES} in three different SM-ESs are presented in Fig. 12(a). V_{Csm} drops slightly until 1.4 s and then rises afterward, and its value keeps around 4.0 kV. V_{ES} decreases briefly until 0.4 s and gradually increases between 0.4 and 1.4 s, with a slower rate of increase after 1.4 s. In Fig. 12(b), the variation of I_L is shown. Before $t = 0.4$ s, it is greater
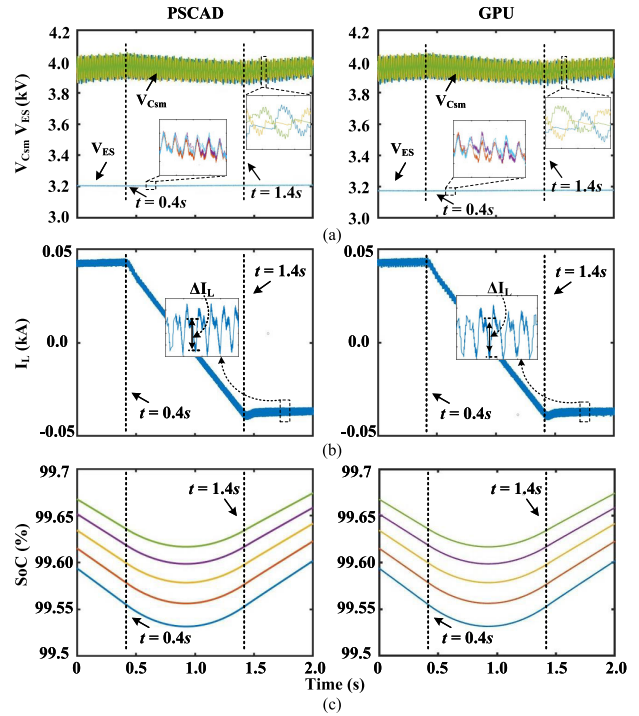
FIGURE 12. GPU and PSCAD^TM simulation results of mode transition: (a) Voltages of capacitor and supercapacitor in SM-ES; (b) DC-DC converter inductor current; (c) SoC of the supercapacitors.

than 0, at approximately 0.04 kA, because the supercapacitors are being discharged at this time. Later on, I_L goes from positive to negative and remains at -0.04 kA at 1.4 s, indicating that the supercapacitor is under the charging state. The current ripple ΔI_L is about merely 0.004 kA which guarantees the CCM. Fig. 12(c) shows the trend of the SoC of supercapacitors with several various initial conditions. The SoC decreases steadily from the beginning to about 1.0 s and then starts to rise, indicating the transition of the energy storage system from a discharging state to a charging state.

The role of the MMC-EES in maintaining power system stability is illustrated in Fig. 13 where system-level results are compared with the scenario without EES. The entire system shown in Fig. 3 operates under steady-state until $t = 1.0$ sec when both wind farms are suddenly disconnected. As a result, MMC_1 and MMC_2 do not receive any active power at their AC sides, but $MMC-EES_1$ and $MMC-ESS_2$ can still deliver the same amount of power to the IEEE 39-bus-test power system after a slight momentary perturbation. Due to their quick response, the AC grid maintains frequency stability, since all 10 generator buses have a frequency close to 60Hz. Meanwhile, the AC bus voltages are also not subjected to obvious changes. In contrast, the output power of the two grid-side MMCs would plunge to zero if they do not have any energy storage units installed, and subsequently, the generator bus frequencies and voltages drop quickly.

The GPU-based simulation shows a tremendous advantage over PSCAD^TM in terms of speed. It takes 890 seconds

TABLE 1. Four-terminal DC system simulation speed comparison.

MMC Level	$N_{sc} = 2$			Speedup		$N_{sc} = 20$			Speedup	
	t_{CPU1}[sec]	t_{CPU2}[sec]	t_{GPU}[sec]	SP_1	SP_2	t_{CPU1}[sec]	t_{CPU2}[sec]	t_{GPU}[sec]	SP_1	SP_2
5	17.48	12.72	45.12	1.4	0.4	43.84	33.79	49.03	1.3	0.9
51	202.38	424.05	58.54	0.5	3.5	575.38	449.68	63.39	1.3	9.1
101	394.52	468.64	67.98	0.8	5.8	1126.73	517.63	75.83	2.2	14.9
201	743.16	567.49	89.23	1.3	8.3	2221.2	676.23	111.95	3.3	19.8
401	1522.66	705.96	143.3	2.2	10.6	4486.68	1052.73	196.82	4.3	22.8
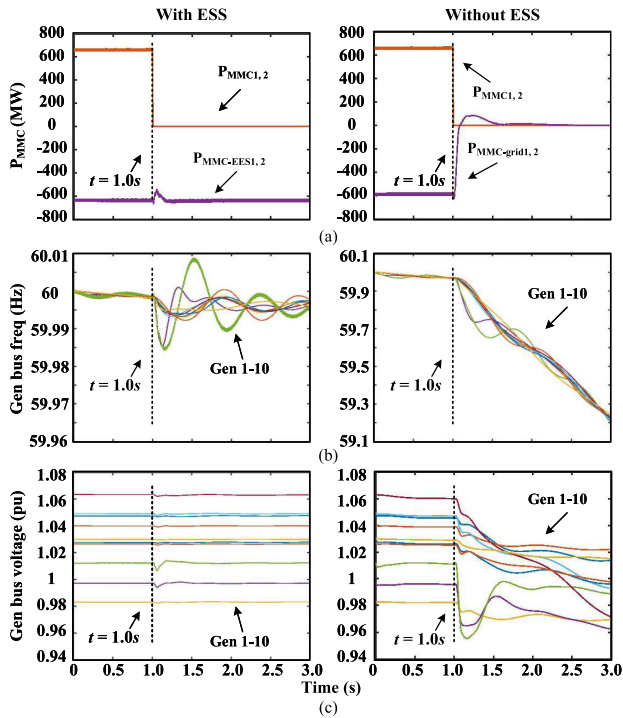
FIGURE 13. System-level simulation result comparison with MMC-EES and MMC without ESS in IEEE 39-bus system: (a) MMC output power; (b) Frequency response of generators; (c) voltages of generator buses.

for PSCAD^{TM} to run a 2-second simulation with merely 1 supercapacitor in each submodule of a 5-level MMC-based HVDC, while GPU only needs around 40 seconds. Therefore, in Table 1, the execution times of GPU (t_{GPU}) are compared with the partitioning algorithm on single-core CPU (t_{CPU1}) and multi-core CPU (t_{CPU2}) for different levels of MMC systems Speedups SP_1 and SP_2 are calculated as the ratios of single-core CPU simulation time to the multi-core CPU and GPU simulation times, respectively. Additionally, the speedup results are analyzed for two different amounts of supercapacitors. For 2 supercapacitors in each SM-ES of a 401-level MMC, SP_1 is 2.2 and SP_2 is 10.6, while for 20 supercapacitors in the same case, SP_2 exceeds 20 and SP_1 is 4.3. Due to the partitioning optimization algorithm and more available hardware resources, speedups are obtained by both multi-core CPU and GPU. It can be seen that the GPU as an acceleration platform achieves an overall faster simulation speed than the CPU, and a higher speedup is gained with either a higher MMC level or more supercapacitor

components in an array. The inherently parallel architecture of GPU fundamentally aligns with the parallelizable nature of MMC system simulations, thus resulting in outstanding acceleration.

VI. CONCLUSION

This paper proposes the detailed nonlinear modeling of MMC with embedded energy storage system for efficient high-fidelity parallel transient simulation of wind energy grid integration. By absorbing or releasing an appropriate amount of power, the MMC which has embedded energy storage in its sub-modules reduces the risk of grid stability arising from stochastic wind power generation. Detailed modeling and control strategy design of the MMC-EES is carried out and applied to a four-terminal HVDC system. The modeling approach as detailed as individual supercapacitors allows their behavior to be monitored, thus providing more accurate information from system simulation for evaluation and energy management. As the high fidelity induced a remarkable computational burden to sequential processing on the CPU, the massively parallel computing advantage of GPU is exploited. Structures with homogeneity are designed and programmed into a single kernel, and manipulation of inhomogeneity is investigated to obtain a more significant acceleration. Different operation scenarios were performed to demonstrate the promising characteristics of the MMC-EES-based HVDC system from both dynamic and static perspectives. Significant speedups over CPU simulation have been achieved and the accuracy of the implementation as well as the computational advantages are verified by comparing the results with off-line simulations on the CPU.

REFERENCES

[1] F. Blaabjerg and K. Ma, "Future on power electronics for wind turbine systems," *IEEE J. Emerg. Sel. Topics Power Electron.*, vol. 1, no. 3, pp. 139–152, Sep. 2013.

[2] X. Han, Y. Qu, P. Wang, and J. Yang, "Four-dimensional wind speed model for adequacy assessment of power systems with wind farms," *IEEE Trans. Power Syst.*, vol. 28, no. 3, pp. 2978–2985, Aug. 2013.

[3] A. Bera, B. R. Chalamala, R. H. Byrne, and J. Mitra, "Sizing of energy storage for grid inertial support in presence of renewable energy," *IEEE Trans. Power Syst.*, vol. 37, no. 5, pp. 3769–3778, Sep. 2022.

[4] T. Kovaltchouk, A. Blavette, J. Aubry, H. B. Ahmed, and B. Multon, "Comparison between centralized and decentralized storage energy management for direct wave energy converter farm," *IEEE Trans. Energy Convers.*, vol. 31, no. 3, pp. 1051–1058, Sep. 2016.

[5] A. Oshnoei, M. Kheradmandi, and S. M. Muyeen, "Robust control scheme for distributed battery energy storage systems in load frequency control," *IEEE Trans. Power Syst.*, vol. 35, no. 6, pp. 4781–4791, Nov. 2020.

[6] J. M. L. Fonseca, S. R. P. Reddy, K. Rajashekara, and K. R. R. Potti, "Reduced capacitor energy requirements in battery energy storage systems based on modular multilevel converters," *IEEE Trans. Ind. Appl.*, vol. 58, no. 6, pp. 7608–7619, Nov. 2022.

[7] L. Qu and W. Qiao, "Constant power control of DFIG wind turbines with supercapacitor energy storage," *IEEE Trans. Ind. Appl.*, vol. 47, no. 1, pp. 359–367, Jan. 2011.

[8] J. Khazaei, "Optimal flow of MVDC shipboard microgrids with hybrid storage enhanced with capacitive and resistive droop controllers," *IEEE Trans. Power Syst.*, vol. 36, no. 4, pp. 3728–3739, Jul. 2021.

[9] S. Wang, D. Vozikis, K. H. Ahmed, D. Holliday, and B. W. Williams, "Comprehensive assessment of fault-resilient schemes based on energy storage integrated modular converters for AC-DC conversion systems," *IEEE Trans. Power Del.*, vol. 37, no. 3, pp. 1764–1774, Jun. 2022.

[10] H. Zhang, F. Mollet, C. Saudemont, and B. Robyns, "Experimental validation of energy storage system management strategies for a local DC distribution system of more electric aircraft," *IEEE Trans. Ind. Electron.*, vol. 57, no. 12, pp. 3905–3916, Dec. 2010.

[11] H. Zhou, W. Yao, M. Zhou, X. Ai, J. Wen, and S. Cheng, "Active energy control for enhancing AC fault ride-through capability of MMC-HVDC connected with offshore wind farms," *IEEE Trans. Power Syst.*, vol. 38, no. 3, pp. 2705–2718, May 2023.

[12] G. Guo et al., "HB and FB MMC based onshore converter in series-connected offshore wind farm," *IEEE Trans. Power Electron.*, vol. 35, no. 3, pp. 2646–2658, Mar. 2020.

[13] N. Herath and S. Filizadeh, "Average-value model for a modular multilevel converter with embedded storage," *IEEE Trans. Energy Convers.*, vol. 36, no. 2, pp. 789–799, Jun. 2021.

[14] N. Herath and S. Filizadeh, "Improved average-value and detailed equivalent models for modular multilevel converters with embedded storage," *IEEE Trans. Energy Convers.*, vol. 37, no. 3, pp. 1998–2008, Sep. 2022.

[15] L. Zhang, Y. Tang, S. Yang, and F. Gao, "Decoupled power control for a Modular-Multilevel-Converter-Based hybrid AC–DC grid integrated with hybrid energy storage," *IEEE Trans. Ind. Electron.*, vol. 66, no. 4, pp. 2926–2934, Apr. 2019.

[16] N. Lin and V. Dinavahi, "Dynamic electro-magnetic-thermal modeling of MMC-based DC–DC converter for real-time simulation of MTDC grid," *IEEE Trans. Power Del.*, vol. 33, no. 3, pp. 1337–1347, Jun. 2018.

[17] V. Dinavahi and N. Lin, *Parallel Dynamic and Transient Simulation of Large-Scale Power Systems: A High Performance Computing Solution.* Cham, Switzerland: Springer, Jan. 2022.

[18] Z. Zhou and V. Dinavahi, "Parallel massive-thread electromagnetic transient simulation on GPU," *IEEE Trans. Power Del.*, vol. 29, no. 3, pp. 1045–1053, Jun. 2014.

[19] N. Lin and V. Dinavahi, "Exact nonlinear micromodeling for fine-grained parallel EMT simulation of MTDC grid interaction with wind farm," *IEEE Trans. Ind. Electron.*, vol. 66, no. 8, pp. 6427–6436, Aug. 2019.

[20] N. Lin and V. Dinavahi, "Parallel high-fidelity electromagnetic transient simulation of large-scale multi-terminal DC grids," *IEEE Power Energy Technol. Syst. J.*, vol. 6, no. 1, pp. 59–70, Mar. 2019.

[21] V. Jalili-Marandi and V. Dinavahi, "SIMD-based large-scale transient stability simulation on the graphics processing unit," *IEEE Trans. Power Syst.*, vol. 25, no. 3, pp. 1589–1599, Aug. 2010.

[22] N. Lin, S. Cao, and V. Dinavahi, "Adaptive heterogeneous transient analysis of wind farm integrated comprehensive AC/DC grids," *IEEE Trans. Energy Convers.*, vol. 36, no. 3, pp. 2370–2379, Sep. 2021.

[23] N. Lin, S. Cao, and V. Dinavahi, "Massively parallel modeling of battery energy storage systems for AC/DC grid high-performance transient simulation," *IEEE Trans. Power Syst.*, vol. 38, no. 3, pp. 2736–2747, May 2023.

[24] N. Lin and V. Dinavahi, "Variable time-stepping modular multilevel converter model for fast and parallel transient simulation of multiterminal DC grid," *IEEE Trans. Ind. Electron.*, vol. 66, no. 9, pp. 6661–6670, Sep. 2019.

[25] J. Sun, S. Debnath, M. Saeedifard, and P. R. V. Marthi, "Real-time electromagnetic transient simulation of multi-terminal HVDC–AC grids based on GPU," *IEEE Trans. Ind. Electron.*, vol. 68, no. 8, pp. 7002–7011, Aug. 2021.

[26] H. Akagi, "Multilevel converters: Fundamental circuits and systems," *Proc. IEEE*, vol. 105, no. 11, pp. 2048–2065, Nov. 2017.

[27] K. B. Oldham, "A Gouy–Chapman–Stern model of the double layer at a (metal)/(ionic liquid) interface," *J. Electroanal. Chem.*, vol. 613, no. 2, pp. 131–138, Feb. 2008.

[28] M. Hagiwara and H. Akagi, "Control and experiment of pulsewidth-modulated modular multilevel converters," *IEEE Trans. Power Electron.*, vol. 24, no. 7, pp. 1737–1746, Jul. 2009.

[29] K. Fung and S. Hui, "Fast simulation of multistage power electronic systems with widely separated operating frequencies," *IEEE Trans. Power Electron.*, vol. 11, no. 3, pp. 405–412, May 1996.

[30] *Whitepaper NVIDIA Tesla V100 GPU Architecture*, NVIDIA Corp, Santa Clara, CA, USA, Aug. 2017.

BINGRONG SHANG (Member, IEEE) received the B.Sc. degree in electronic information science and technology from Henan University, Kaifeng, China, in 2020, and the M.Sc. degree in electrical and computer engineering from the University of Alberta, Edmonton, AB, Canada, in 2023. Her research interests include electromagnetic transient simulation of power systems and power electronics, real-time emulation, and adaptive compute acceleration using heterogeneous hardware.

NING LIN (Member, IEEE) received the B.Sc. degree in applied electronics engineering and the M.Sc. degree in electrical engineering from Zhejiang University, Hangzhou, China, in 2008 and 2011, respectively, and the Ph.D. degree in energy systems from the University of Alberta, Edmonton, AB, Canada, in 2018. From 2011 to 2014, he was an Engineer in substation automation, FACTS, and HVdc control and protection. He is currently a Senior Power Systems Consultant with Powertech Labs Inc. His research interests include ac/dc grids, electromagnetic transient simulation, hardware emulation, power system stability analysis, and heterogeneous high-performance computing of power electronics and power systems on GPU.

VENKATA DINAVAHI (Fellow, IEEE) received the B.Eng. degree in electrical engineering from the Visvesvaraya National Institute of Technology (VNIT), Nagpur, India, the M.Tech. degree in electrical engineering from the Indian Institute of Technology (IIT) Kanpur, India, and the Ph.D. degree in electrical and computer engineering from the University of Toronto, ON, Canada. He is currently a Professor with the Department of Electrical and Computer Engineering, University of Alberta, Edmonton, AB, Canada. His research interests include real-time simulation of power systems and power electronic systems, electromagnetic transients, device-level modeling, artificial intelligence machine learning, large-scale systems, and parallel and distributed computing. He is a fellow of the Engineering Institute of Canada (EIC) and the Asia–Pacific Artificial Intelligence Association (AAIA). He is a registered Professional Engineer in the Province of Alberta.

● ● ●